



Photocatalytic mediated destruction of 2-chlorobiphenyl by a ZnO-[10%]BiOI *p-n* heterojunction: effect of some process parameters

D. C. Ashiegbu¹ · H. Potgieter^{1,2}

Received: 22 September 2022 / Revised: 5 July 2023 / Accepted: 8 October 2023 / Published online: 30 October 2023
© The Author(s) 2023

Abstract

This study involved the synthesis, characterization, and application of various photocatalysts and heterojunctions using zinc oxide (ZnO), tungsten trioxide (WO₃), and bismuth oxyiodide (BiOI) for the photo-abatement of 2-chlorobiphenyl (2CBP). Scanning electron microscopy revealed a variety of morphologies for all composites, while energy-dispersive X-ray spectroscopy only identified reference elements and X-ray diffraction patterns displayed crystalline patterns with no impurity peaks. The absorbance of the heterostructures exhibited slight red shifts as WO₃ and BiOI were etched into ZnO. Except for ZnO-[10%]WO₃, the band gaps of all composites decreased/narrowed as the doping of WO₃ and BiOI into ZnO increased. Nitrogen sorption isotherms revealed that almost all the prepared materials had a Type IV isotherm, and the heterostructures showed higher surface area measurements compared to the undoped composites. The ZnO-[10%]BiOI heterojunction, which displayed the best photoactivity, was further investigated to analyze the influence of some operating conditions. Results revealed that the initial pollutant concentration influenced the degree of photodegradation, which decreased with increased initial 2CBP concentration. The optimum photocatalytic performance was detected at neutral pH. The pseudo-first order kinetic model showed that doubling the heterojunction's weight increased the rate constant from 0.0054 to 0.0089 min⁻¹, while increasing the pH to 11.3 resulted in an 18-fold reduction. Overall, the study demonstrated the potential application of ZnO-[10%]BiOI heterostructure as a highly effective photocatalyst for recalcitrant contaminants in water.

Keywords Photodestruction · Doping · Heterojunction photocatalyst · Polychlorinated biphenyls · Simulated sunlight

Introduction

Polychlorinated biphenyls (PCBs) are manmade chemicals that have various appearances such as solids or oily liquids, clear or sometimes yellow color and with no smell or taste. PCBs exhibit chemical stability, meaning they are resistant to strong acids and bases, nonflammable, thermally stable, and not easily oxidized or reduced (Hong et al. 1998). They are categorized as enduring organic

toxins due to their hazardous nature and chemical stability (Dasary et al. 2010). Additionally, they have low electrical conductivity and are soluble in a broad range of organic solvents. Pure PCBs are either non-crystalline solids or liquids at room temperature, while commercial mixtures are primarily viscous liquids. However, mixtures with high chlorine content can be solid. As of 2016, the United Nations Environment Program (UNEP) reported that approximately 17 million tons of liquids and equipment containing PCBs remained to be addressed to accomplish the goals of the Stockholm Convention, which aims to eradicate these compounds by 2028 (Robertson et al. 2018). This represents 83% of the total amount of PCB-containing materials that were produced and used globally (Robertson et al. 2018; Šrédlová and Cajthaml 2022). As a result of their characteristics, particularly their durability, vapor pressures, and KOW, they have become widely present in the environment, having been detected in various

Editorial responsibility: Dai-Viet N. Vo.

✉ D. C. Ashiegbu
darlington.ashiegbu@wits.ac.za

¹ School of Chemical and Metallurgical Engineering, University of the Witwatersrand Johannesburg, Private Bag X3 PO Wits 2050, Johannesburg, South Africa

² Department of Natural Science, Manchester Metropolitan University, Chester Street, Manchester M1 5GD, UK



biota and environmental substances across all areas of the world and in all types of ecosystems.

Despite ceasing production and discontinuation of industrial use, PCBs continue to be present as concerning pollutants at hazardous waste sites and within the environment. Long-term exposure to PCBs can result in chronic toxicity that may cause harm to the body organs, central nervous system, and reproductive system (Dasary et al. 2010). Currently, the United States Environmental Protection Agency (EPA) has set a zero maximum contaminant level goal (MCLG) as well as a maximum contaminant level (MCL) of 0.5 parts per billion (ppb) for polychlorinated biphenyls (PCBs) in municipal water systems (Liang et al. 2014).

Various methodologies have been devised for the remediation of sites contaminated with PCBs. These include biodegradation, incineration, solvent extraction, adsorption, and chemical treatment with nanoscale zero-valent iron, but these approaches might not be totally productive (Jing et al. 2018; Šrédlová and Cajthaml 2022). Incineration is the most used method for managing waste containing elevated levels of PCBs, particularly dielectric oils. However, this approach has its drawbacks, including environmental hazards such as dioxins and benzofurans, as well as the high cost of managing, transporting, and disposing of the contaminated residue that remains after incineration (Lin et al. 1995; Asilian et al. 2010). Biodegradation is a slow process that necessitates careful monitoring to ensure that the desired outcome is achieved. Solvent extraction is costly and may require the use of hazardous solvents. Adsorption, on the other hand, necessitates careful monitoring to ensure that the adsorbent does not become saturated with PCBs and lose its efficacy. Studies have proposed various approaches to manage waste containing high concentrations of PCBs, including combining several processes such as sorption on activated carbon, followed by heat treatment, or supercritical oxidation. However, these approaches tend to be costly (Jing et al. 2018; Šrédlová and Cajthaml 2022). As PCBs are persistent and adversely impact the environment, their destruction is crucial for environmental protection.

Advanced Oxidation Processes (AOPs) have been extensively utilized for the removal of organic toxins, due to their ability to generate hydroxyl radicals ($\cdot\text{OH}$), superoxide anions ($\cdot\text{O}^{2-}$), and electron/hole (e^-/h^+) pairs in-situ, which can transform pollutants into less and non-toxic (Osman et al. 2023). Some of the commonly used AOPs include photo-Fenton catalysis, UV-based AOPs, ozone-based AOPs, hydroxyl radical-based AOPs, super critical water oxidation processes and photocatalysis (Deng and Zhao 2015; Liu et al. 2019; Litter and Quici 2011). While various AOPs have been utilized in the abatement of various organic contaminants, photocatalysis has appeared as the

most prospective and eco-friendly option because its high ability in catalyzing the destruction of organic pollutants into environmentally benign products (Malik et al. 2022). However, traditional photocatalysts such as TiO_2 , ZnO , and WO_3 have limitations such as high carrier recombination, wide bandgap, photocorrosion, vulnerability to dissolution in acidic media, and absorption only in UV light, which restricts their modern applications (Ashiegbu et al. 2023; Malik et al. 2022). Therefore, the development of new and improved photocatalysts is crucial for the efficient destruction of pollutants like 2CBP.

There has been a rising interest in enhancing the photocatalytic performance of conventional photocatalysts, including TiO_2 , ZnO , and WO_3 , in recent years. These materials have certain drawbacks, such as high carrier recombination rates, wide bandgaps, photocorrosion during prolonged illumination, dissolution in acidic media, and only absorbing UV light, which limit their usage in current applications. Extensive research is currently being conducted to develop new approaches for modifying photocatalysts to address the limitations mentioned above. Incorporating nonmetal and metal elements through doping is a viable technique that can tune down the energy gap, enhance the charge carrier migration, and reposition the threshold of photon absorption to the visible spectrum (Mirzaeifard et al. 2020). In addition to metal doping, semiconductor coupling to create heterojunctions has been confirmed to enhance the migration of charge carriers, which prolongs the lifespan of the photocarriers and ultimately decreases recombination (Lee et al. 2016). Furthermore, researchers have explored hydrogenation techniques such as annealing in a hydrogen-rich environment or attaching ZnO onto carbon nanostructures as means of enhancing the photocatalytic capabilities of ZnO (Kumar and Rao 2017, 2015). These novel techniques hold the potential for providing effective solutions to enhance the efficacy and functionality of ZnO -based photocatalysts in various industrial and environmental applications (Ibhadon and Fitzpatrick 2013; Yan et al. 2013). Implementing these strategies cause the creation of a Schottky barrier at the interface between the photocatalyst and co-catalyst (metal or metal oxide), a reduced bandgap, a suppression of charge carrier recombination, improved light absorption properties, enhanced structural stability, the induction of localized surface plasmon resonance (SPR), and an overall improved photocatalytic efficiency (Pirhashemi et al. 2018; Jiang et al. 2017; Wang et al. 2017). As such, it is crucial to modify and enhance photocatalysts for better and efficient photo-activity.

This research investigates the photodestruction of 2CBP using ZnO , WO_3 , BiOI , and ZnO -based heterojunction photocatalysts with varying loadings of WO_3 and BiOI . The composite that exhibited the best pollutant removal



performance was used to examine the impact of process conditions such as pH, catalyst weight, and contaminant levels on the photodestruction process. Considering the stability and challenging destruction mechanism of 2CBP, previous studies focused on very low concentrations ranging from 0.025 ppm to 3.8 ppm. However, the present study selected a higher concentration of 10 ppm. The ZnO-[10%]BiOI heterostructure demonstrated enhanced photo-activity due to several factors, such as the establishment of a *p-n* interface, effective absorption of both visible and UV light, and effective charge carrier separation. These findings indicate that ZnO-[10%]BiOI could be applied as a functional photocatalyst for removing refractory contaminants from water.

This research was carried out at the University of Witwatersrand in Johannesburg South Africa, as part of the PhD research of the corresponding author. The study took place between the months of January to April in 2021.

Materials and methods

Materials

The materials for the experiments were obtained from various sources. Potassium iodide ($KI \geq 99\%$), bismuth nitrate pentahydrate ($Bi(NO_3)_3 \cdot 5H_2O \geq 98\%$), ammonium metatungstate ($(NH_4)_6H_2W_{12}O_{40} \geq 85\%$), oxalic acid (99%), and 2-chlorobiphenyl (2CBP $\geq 99\%$) were provided by Sigma-Aldrich South Africa. Zinc acetate dehydrate [$\geq 99\%$] and ethanol ($\geq 99\%$) were obtained from Associated Chemical Enterprises South Africa, while methanol ($\geq 99\%$) was acquired from the School of Chemistry at University of the Witwatersrand. All chemicals and solvents used in the investigation were of analytical reagent grade and were not further purified before use. Deionized (DI) water was used for all sample preparations, which was purified using a Millipore system. The solution pH was adjusted with 0.1 M HCl and 1 M NH_4OH . To prepare a 1000 ppm stock solution of 2CBP, methanol and water were mixed in an 85:15 ratio under continuous and constant stirring. The standard solution was further diluted to achieve the working concentration of 10 ppm for the study.

Synthesis of undoped photocatalysts and heterojunction photocatalysts

As previously reported, a sol-gel route was utilized to fabricate the ZnO nanoparticles (Ashiegbu et al. 2022). ZAD [$Zn(CH_3COO)_2 \cdot 2H_2O$] was firstly dissolved in alcohol and then added to a reactor attached to a reflux system and thermostatic bath. The solution was then refluxed at 60 °C with

aggressive agitation for 30 min which resulted in a colorless solution. Oxalic acid was dissolved in ethanol and gradually poured (in drops) into the ZAD solution, effecting the formation of gels which were left to reflux for an hour at 50 °C. The gel was allowed to cool and then dried all night. The resulting sample was roasted at 500 °C to produce ZnO composite.

A facile hydrothermal approach was used to produce WO_3 nanoparticles. Deionized water was used to dissolve ammonium metatungstate (AMT), and the mixture was subsequently poured into an autoclave. Following the reaction, the autoclave was transferred to an oven at 120 °C for 18 h. The sample was then filtered, washed with water and ethanol, and left to air-dry. The final composite was roasted for 2 h at 500 °C to obtain WO_3 .

A hydrothermal process was utilized to synthesize BiOI nanoplates, using bismuth nitrate pentahydrate and potassium iodide as starting materials. Bismuth nitrate pentahydrate was dissolved in alcohol amidst stirring for 30 min, while KI was dissolved in DI. Potassium iodide was then slowly added in droplets to the former while stirring. The observed deep red solution was subsequently transferred into an autoclave and subjected to 18 h of heating at 130 °C. The reactor was retrieved and allowed to cool gradually. The emulsion was filtered and rinsed with water and alcohol. The Teflon of the autoclave was also rinsed with DI and alcohol. The product was dried and ground to obtain BiOI nanoplatelets.

To prepare ZnO-[X] WO_3 heterojunctions at varying weight loadings of 5%, 10%, and 20%, ZnO was dissolved in water while maintaining the pH of the mixture at 6.5 using ammonium hydroxide. AMT was added to the blend and agitated for 15 h. To obtain the ZnO-[X] WO_3 heterojunctions, the precipitate was separated through filtration and subsequently washed multiple times with deionized water and alcohol. Then, it was air-dried, collected, and ground in an agate mortar. The powdered material was subjected to 3 h of heating at 500 °C.

To synthesize ZnO-[X]BiOI heterojunctions, a suspension of ZnO was prepared in deionized water. Bismuth nitrate pentahydrate was added to ethanol and vigorously stirred, then emptied into the ZnO emulsion and the blend was agitated continuously. Next, potassium iodide was dissolved in DI and gradually poured into the mixture while stirring vigorously. The reaction mixture was stirred for 3 h and then separated by a centrifugal separator at 4000 rpm for 15 min. The resulting product was dried for 18 h in ambient air and ground in an agate mortar to obtain the ZnO-BiOI based heterostructure photocatalyst (Fig. 1).



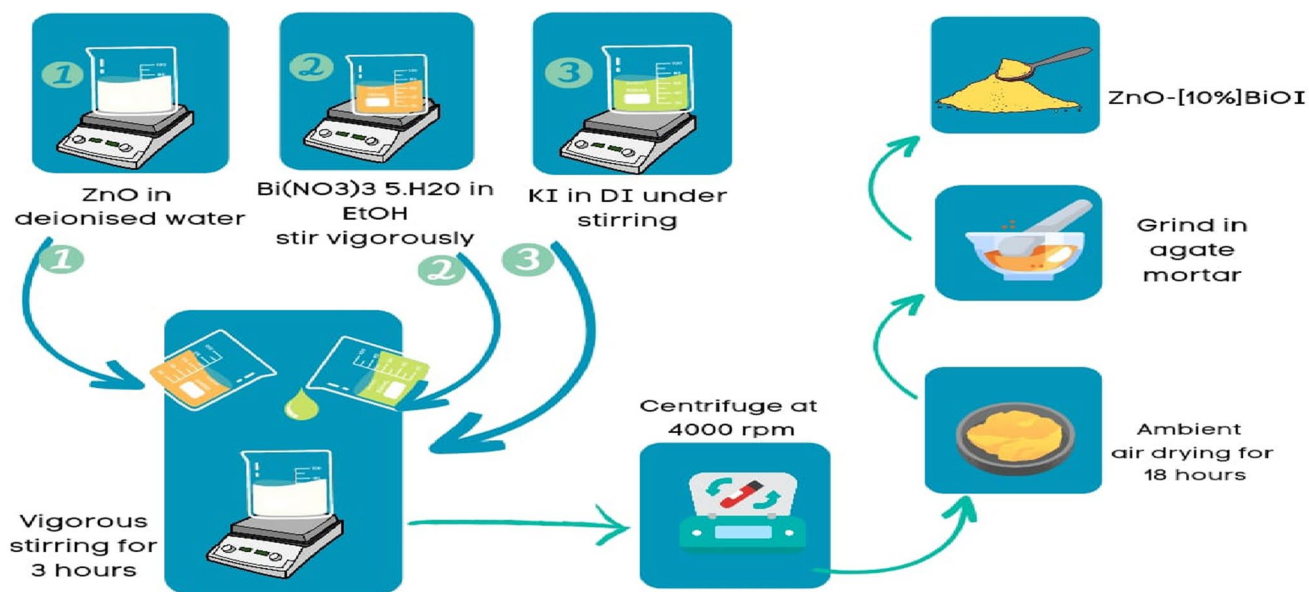


Fig. 1 Synthesis of ZnO-[X]BiOI heterojunction

Photocatalytic process

To evaluate the performance of the materials, the photodegradation of 2-chlorobiphenyl (2CBP) was carried out under simulated solar radiation. A solution containing 10 ppm of 2CBP in a methanol–water mixture was prepared and placed on a stirrer plate right beneath the solar simulator. The composites were poured into the solution and agitated without light for 30 min to equilibrate adsorption–desorption. The solution's pH was regulated with hydrochloric acid and ammonium hydroxide, and the suspensions were continuously stirred during the experiment. The performance of the photocatalysts were assessed using a solar radiation simulator, and the beaker surface was enclosed to avert evaporation. Samples were taken at specified intervals and filtered through a syringe equipped with a 0.22 μm membrane filter to isolate the photocatalysts. To prevent light exposure and ensure the integrity of the filtered samples before analysis following irradiation, they were kept in a refrigerator and placed inside an aluminum foil lined dark box.

Results and discussion

Photocatalysts and heterojunction characterization

Morphological analysis and elemental composition of the nanocomposites were determined using a Carl Zeiss Sigma FE-SEM coupled with an Oxford X-act EDS. The optical analysis was performed with a UV 1800 Shimadzu

UV–Vis Spectrophotometer while a Bruker D2 XRD instrument was used to measure the crystalline phases. Mean crystallite sizes of the composites were measured via the Debye–Scherrer relation from diffraction peaks and band gap measurements were determined using Tauc plots based on UV–vis spectra. A Micrometrics TriStar 3000 was used to determine surface area measurements and isotherms. For the separation of suspended particles during reactions, a Hettich ROTOFIX Benchtop Centrifuge was used, and pH levels were obtained with an OHAUS Starter 3100 pH meter. The photocatalytic degradation of 2CBP

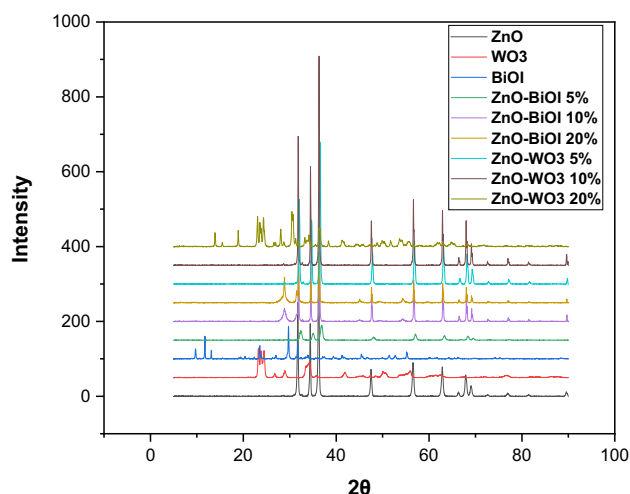


Fig. 2 XRD patterns of undoped photocatalysts and heterojunction photocatalysts

was performed using a GC–MS QP 2010 coupled with an Rxi-5 ms column and an AM 1.5G 100 mW/cm² as light source.

X-ray diffraction

As reported previously, the ZnO nanoparticles showed a hexagonal wurtzite structure, with intense and strong peaks detected at 2θ values of 31.7°, 34.4°, 36.1°, 47.3°, 56.3°, 62.6°, 66.3°, 67.9°, and 69.1°, corresponding to the (100), (002), (101), (102), (110), (103), (200), (112), and (201) crystal planes, respectively (Ashiegbu et al. 2022). The diffraction peaks observed in Fig. 2 indicated a high degree of crystallinity in the pure ZnO. The BiOI sample was found to exhibit BiOI tetragonal phase. Along with the pristine phase of BiOI, mixed phases such as Bi₅O₇I and Bi₇O₉I₃ were also identified in the sample. The diffraction peaks at 10°, 30°, 34°, 46°, and 56° were observed in the sample, which corresponded to the (001), (102), (110), (200), and (212) diffraction planes, respectively. This suggests that the sample has a high level of crystallinity. From the WO₃ pattern, it was confirmed that the triclinic phase of WO₃ was present. The non-existence of any impurity peaks in the pattern indicated that the sample was pure and had been synthesized successfully. The peaks that were detected at 23.26°, 24.47°, 26.79°, 28.95°, 34.20°, 49.98°, and 55.89° corresponded to the (001), (110), (101), (200), (201), (220), and (202) diffraction planes, respectively. It was observed in the ZnO-[5%] BiOI loaded sample that there was no detection of BiOI peaks within the ZnO lattice, which may be ascribed to the low loading of BiOI on the ZnO surface and the low detection limit of the instrument. However, in the sample with a 10% loading, a peak at 29° was observed in the pattern, which corresponded to the 102-diffraction plane of BiOI. This suggested that BiOI was integrated within the ZnO lattice. This observed peak at 29° was more intense at 20% loading. Overall, the XRD patterns of all three samples confirmed sample purity, good preparation method, and the uniform spread of BiOI on the ZnO surface. The XRD pattern of all ZnO-[X]WO₃ samples showed their crystalline nature, exhibiting the typical triclinic phase of WO₃ and hexagonal wurtzite structure of ZnO (as illustrated in Fig. 2). By using the Debye–Scherrer equation with the FWHM obtained from the diffraction peaks of the synthesized photocatalysts, their average crystallite sizes were determined:

$$D = K \left[\frac{\lambda}{\beta \cos \theta} \right] \quad (1)$$

where k is a constant that depends on the shape of the crystal grains and is typically taken as 0.9. In this equation, $\lambda = 1.54056$ nm (diffraction wavelength), θ is the Bragg

diffraction angle of the XRD peak, while β is the measured broadening diffraction line peak at an angle 2θ at half its peak intensity, expressed in radians.

The mean crystallite sizes of WO₃, BiOI and ZnO were measured as 13, 40 and 37.6 nm respectively (Supplementary Information Table S4). The mean crystal sizes of the ZnO-BiOI based heterostructures were determined to be 16.4, 31, and 45 nm for 5%, 10%, and 20% BiOI loading, respectively. The increase in BiOI loading resulted in an increase in the average crystal size, possibly due to the penetration of the tetragonal BiOI into the hexagonal wurtzite crystal structure of ZnO, leading to a collapse of crystal growth. This phenomenon may have contributed to the small crystallite size of the ZnO-[5%]BiOI sample in contrast to the other composites. The ZnO–WO₃ based heterojunctions exhibited mean particle sizes of 35.4, 49 and 31 nm corresponding to 5, 10 and 20% weight loadings.

Scanning electron microscopy

A FE-SEM was employed to examine the morphologies of the prepared materials. The ZnO nanoparticles exhibited elevated porosity and aggregation because of the high temperature chemical reactions during the synthesis process at 500 °C (Fig. 3a). The resulting compact morphology was on account of the complete disintegration of the organometallic precursor. The morphology of the BiOI composite was irregular and plate-like and caused increased ions diffusion rate (Fig. 3b), which may have been influenced by the hydrothermal approach and the solvents utilized. The WO₃ sample exhibited a blend of non-homogeneous nanorods with high agglomeration and pointed tip morphology (see Fig. 3c), which may have resulted from prolonged hydrothermal reaction time and subsequent high temperature calcination (500 °C).

Observations from the SEM micrographs of the ZnO-BiOI based heterostructures indicated modifications in the morphology of the pure ZnO. The non-uniform surfaces were apparent, and as the BiOI doping increased, the rods and rectangular plates penetrated the ZnO material, at 5% loading of BiOI (Fig. 3d). With 10% loading, a greater degree of penetration and the inception of agglomeration was noticeable, with the formation of unevenly shaped aggregates and some plates (as shown in Fig. 3e). The 20% doped sample exhibited more aggregation, causing a morphology reminiscent of a sponge with pores. This effect may have been caused by further wrapping of the ZnO and BiOI aggregates (Fig. 3f). These observations suggest that the morphology of the heterostructures is significantly influenced by the amount of BiOI loading. SEM images of the ZnO–WO₃ based heterostructures



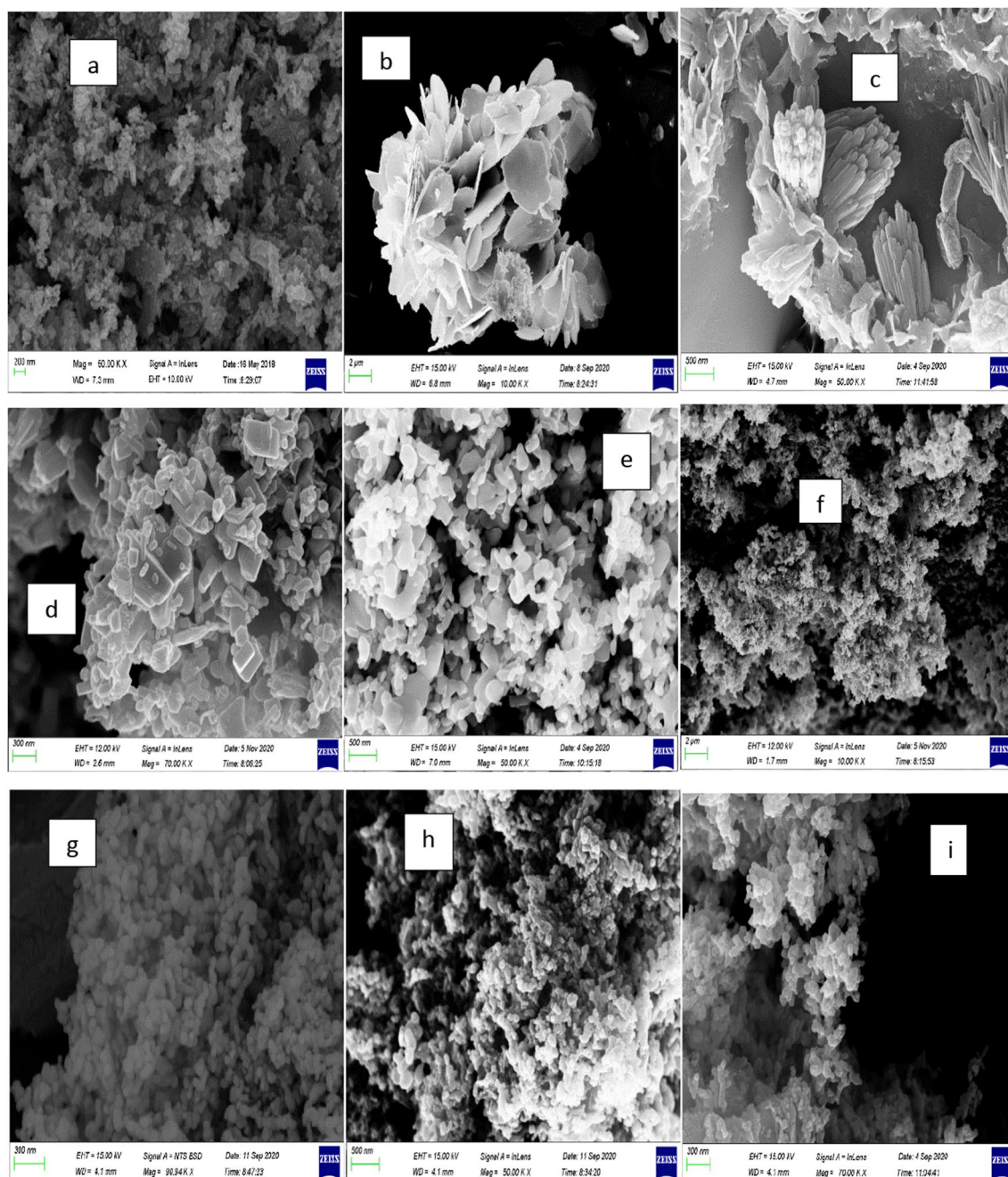


Fig. 3 SEM analysis: **a** ZnO; **b** BiOI; **c** WO₃; **d** ZnO-[5%]BiOI; **e** ZnO-[10%]BiOI; **f** ZnO-[20%]BiOI; **g** ZnO-[5%]WO₃; **h** ZnO-[10%]WO₃; **i** ZnO-[20%]WO₃

revealed agglomeration without any uniform morphology (Fig. 3g–i). Upon closer examination, nodular morphology was evident in all three samples. With an increase in WO₃ loading, more aggregation was evident. This outcome

might be ascribed to the procedure for preparation and precursors, which caused the formation of very thick clusters of small, interconnected grains. The sample with 20% wt WO₃ showed the optimum degree of aggregation. In

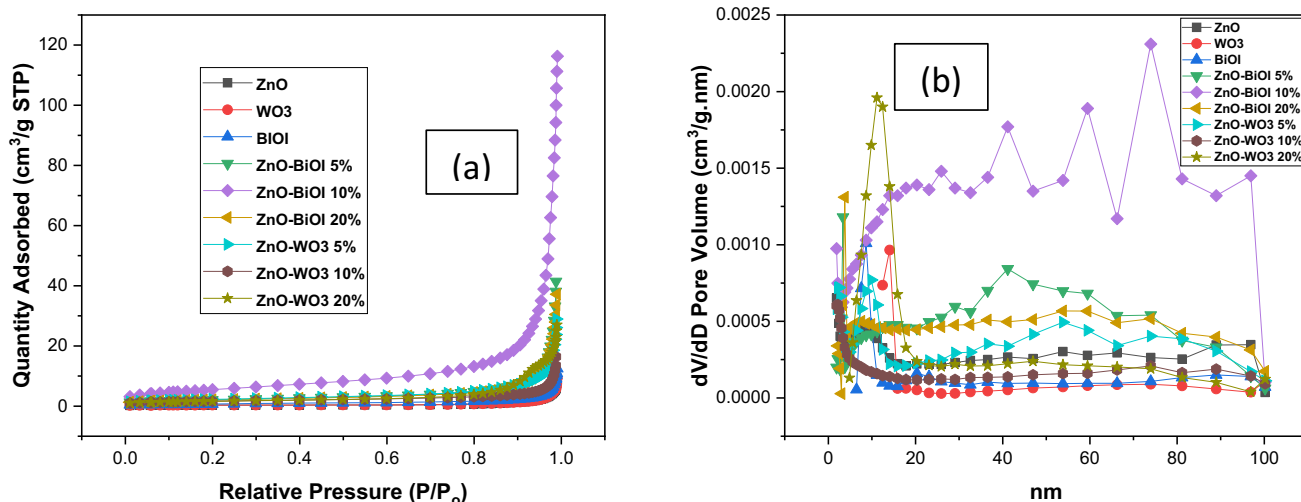


Fig. 4 **a** N_2 adsorption–desorption isotherms of the undoped photocatalysts and heterojunction photocatalysts; **b** BJH pore size analysis

general, the morphologies of all three materials did not display substantial variations as the doping concentration increased in contrast to the SEM micrographs of undoped ZnO and WO_3 .

The results of the EDS analysis indicated only the expected elements along with their corresponding stoichiometric ratios, as depicted in Figure S1.

Surface area and BJH pore analysis

The effective surface areas of the composites were ascertained via the N_2 sorption isotherm and Barret-Joyner-Halender (BJH) pore size distribution curve analyses, as reported elsewhere (Ashiegbu et al. 2022). The surface area data were subsequently compared to the IUPAC classification. The specific surface area of the synthesized photocatalysts and heterojunction photocatalysts (ZnO, BiOI, WO_3 , ZnO-[5%]BiOI, ZnO-[10%]BiOI, ZnO-[20%]BiOI, ZnO-[5%] WO_3 , ZnO-[10%] WO_3 , and ZnO-[20%] WO_3), were determined as 1.93, 2.61, 1.08, 7.31, 19.79, 7.30, 7.84, 5.69, and 5.57 m^2/g , respectively. The nitrogen sorption isotherm analysis revealed that almost all the prepared materials showed Type IV isotherms and were mesoporous, except for ZnO, which displayed a Type V isotherm (Fig. 4a). Hysteresis was not evident in most of the isotherms, except for ZnO, ZnO-[20%]BiOI, ZnO-[20%] WO_3 , and WO_3 , which presented Type H_{III} hysteresis. The BJH pore analysis showed a combination of mesopores and macropores, with ZnO-[5%

BiOI and ZnO-[10%]BiOI exhibiting more macropores than mesopores (Fig. 4b). Although the construction of heterojunctions resulted in an increase in surface area measurements, this accretion did not show a consistent trend.

Optical properties and bandgap measurements

The absorption properties of the materials were determined using a UV–visible spectrophotometer. The spectra were obtained at ambient temperature, covering a range of 200–900 nm. To calculate the E_g , Tauc's plots were used with the Kubelka–Munk equation (Eq. 2). The linear part of the plot of $(\alpha h\nu)^2$ versus photon energy was extrapolated, and the bandgap was obtained using the following equation:

$$\alpha h\nu = A(h\nu - E_g)^n \quad (2)$$

where the absorption coefficient is α , a constant A , Planck's constant h , photon frequency ν , band gap energy E_g , and exponent n (equal to either 1/2 or 2 depending on the direct or indirect nature of the transition). The band gap energy was determined experimentally by extrapolating the linear portion of the plot of $(\alpha h\nu)^2$ versus $h\nu$ to obtain the value at zero frequency.

Fig. S2a–h displays the absorbance and Tauc plots of the bare photocatalysts and heterostructure photocatalysts. The absorbance of ZnO, BiOI, and WO_3 , as well as their respective composite materials (ZnO-[5%]BiOI, ZnO-[10%



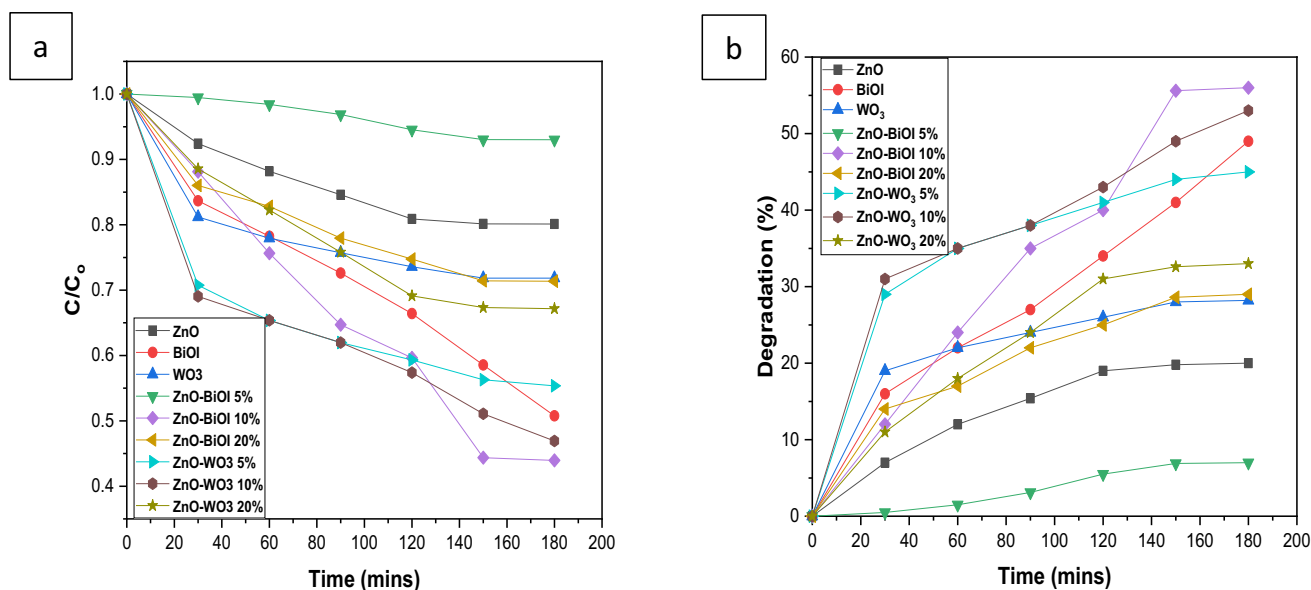


Fig. 5 Photodestruction plots of: **a** 2-chlorobiphenyl; **b** destruction efficiency

BiOI, ZnO-[20%]BiOI, ZnO-[5%]WO₃, ZnO-[10%]WO₃ and ZnO-[20%]WO₃ were detected at wavelengths of 373, 371, 465, 376, 378, 380, 376, 377, and 380 nm, respectively. The absorption tail of BiOI was also detected above 600 nm, which aligns with the observations made by Qu et al. (2020). The absorption tail observed in the optical spectrum for WO₃ nanoparticles is commonly ascribed to the existence of pentavalent tungsten (W^{5+}) on the nanoparticle surface. This broad absorption is induced by the trapping of photoexcited electrons at specific sites in the WO₃, as reported in the literature (Boruah et al. 2020). All heterostructures exhibited slight red shifts in their absorption spectra.

The calculated band gap values for the pure photocatalysts (ZnO, BiOI, WO₃) were 3.24, 1.23, and 2.4 eV, respectively. As the BiOI loading in the ZnO-(X)BiOI heterostructures increased, the bandgaps reduced. A reduction in the bandgap of ZnO was observed at 5% wt BiOI (3.08 eV). The bandgap further decreased to 3.0 eV at 10% BiOI wt loading while the most significant bandgap reduction was observed at 20% wt loading (2.20 eV). This bandgap reduction correlated with a redshift in the absorption spectra of each composite. A calculated energy gap of 2.56 eV was measured for the ZnO-[5%]WO₃ material, demonstrating a narrowing of the energy gap from the bare ZnO (3.24 eV). At 10% wt WO₃ loading, energy level defects may have formed in the forbidden band, causing the energy gap to increase to

3.16 eV, although this value falls beneath the threshold of the bare ZnO bandgap of the. This also accounts for the band gap reduction down to 2.17 eV observed in the sample doped with 20% wt WO₃. These observations align with those of Adhikari et al. (2015).

Photocatalytic performance evaluation

The photocatalytic degradation of 2CBP (Fig. 5a) was evaluated using the as-synthesized composites, which displayed varying degrees of photo-efficiencies. The undoped photocatalysts, including ZnO, WO₃, and BiOI, demonstrated efficiencies of 20%, 28%, and 49%, respectively, under similar reaction conditions. The superior performance of BiOI, which exhibited the highest photodestruction of 2CBP among the bare photocatalysts, is ascribed to the fast disengagement of e^-/h^+ in the BiOI before recombination, as well as its small bandgap.

The heterojunction composites ZnO-[5%]BiOI, ZnO-[5%]WO₃, ZnO-[10%]BiOI, ZnO-[10%]WO₃, ZnO-[20%]BiOI and ZnO-[20%]WO₃ demonstrated efficiencies of 7%, 45%, 56%, 53%, 28% and 33%, respectively. The most significant photocatalytic performances were observed in ZnO-[10%]BiOI and ZnO-[10%]WO₃, which showed 56% and 53% efficiencies, respectively. ZnO-[10%]BiOI exhibited nearly twice the activity of ZnO-[20%]BiOI (28%), while



Table 1 Comparison with previous studies

Catalyst	Synthesis method	Pollutant	Pollutant concentration (ppm)	Efficiency (%)	References
TiO ₂	Purchased	2CBP	3.8	63	Hong et al. (1998)
TiO ₂	Purchased	2CBP	0.265	90	Huang et al. (1996)
TiO ₂	Purchased	2CBP	0.025	0	Carey et al. (1976)
TiO ₂	Purchased	2CBP	3.8	67	Wang et al. (1999)
TiO ₂	Purchased	2CBP	0.08	23	Zhang et al. (1993)
ZnO-[10%]BiOI	Direct and facile	2CBP	10	56	This study

ZnO-[10%]WO₃ exhibited better degradation efficiency than ZnO-[20%]WO₃ (33%). However, ZnO-[20%]BiOI and ZnO-[20%]WO₃ showed poor photocatalytic performance, which can be ascribed to over-doping leading to the creation of recombination centers, in addition to incident light piercing depth exceeding the space charge layer, resulting in rapid recombination of the photoinduced charge carriers (Gnanaprakasam et al. 2015; Khatamian et al. 2012). The enhanced performance of the ZnO-[10%]BiOI heterojunction is ascribed to various factors such as enhanced light absorption, better separation of charges, reduced bandgap, presence of exposed reactive facets, and a larger surface area. These factors caused the production of more OH[•], which enhanced the number of reaction sites (Yan et al. 2022).

The incorporation of BiOI within the lattice of ZnO enabled photosensitization due to its visible spectrum properties and improved performance. This can be credited to the fast charge migration channel between BiOI and ZnO, which caused high-contact areas and improved the overall efficiency of the photocatalyst. It is suggested that a decline

in photocatalytic performance by ZnO-[20%]BiOI and ZnO-[20%]WO₃ heterojunction composites can be ascribed to several factors such as reduced separation efficiency of photoinduced charge carriers, decreased active sites, and the tendency of BiOI to agglomerate (Ashiegbu et al. 2023; Yan et al. 2022).

Table 1 shows previously reported results from photocatalytic destruction of 2CBP. Previous studies have been mainly on the destruction of 2CBP by application of commercially purchased TiO₂ (P25). This study destroyed 2CBP by applying a fabricated heterojunction comprising optimum doping of BiOI into the ZnO lattice. In addition, previously reported data show that previous studies worked with considerably lower concentrations than this study. The performance of the ZnO-[10%]BiOI confirms that it can be suitably applied to destroy recalcitrant pollutants and for wastewater treatment.

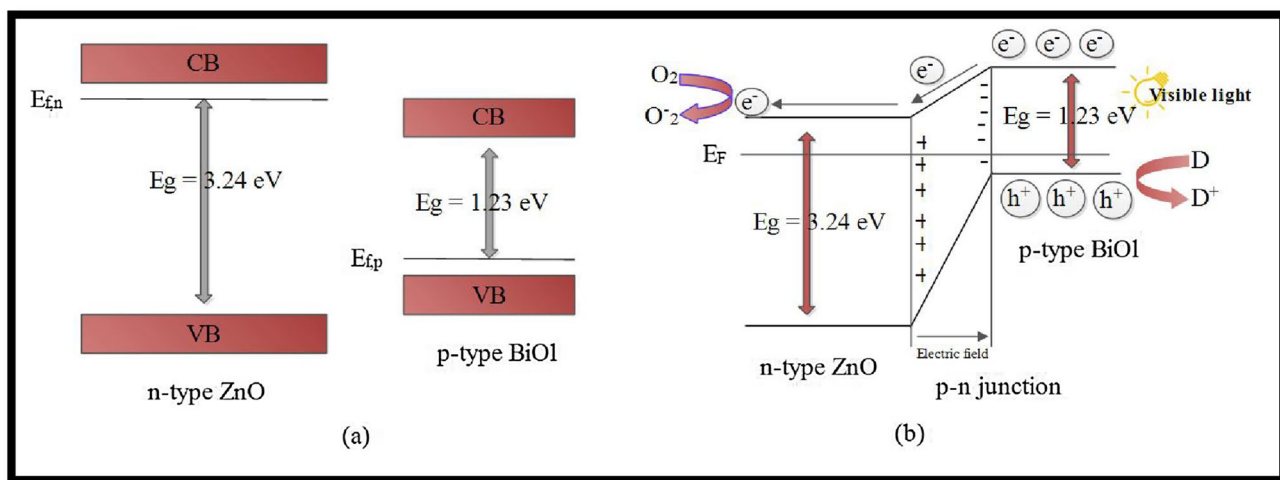


Fig. 6 Suggested band energy diagram of ZnO and BiOI: **a** before contact; **b** after interfacial contact, formation of *p-n* junction and charge migration process of ZnO-[10%]BiOI heterostructure under solar irradiation (Ashiegbu et al. 2022)



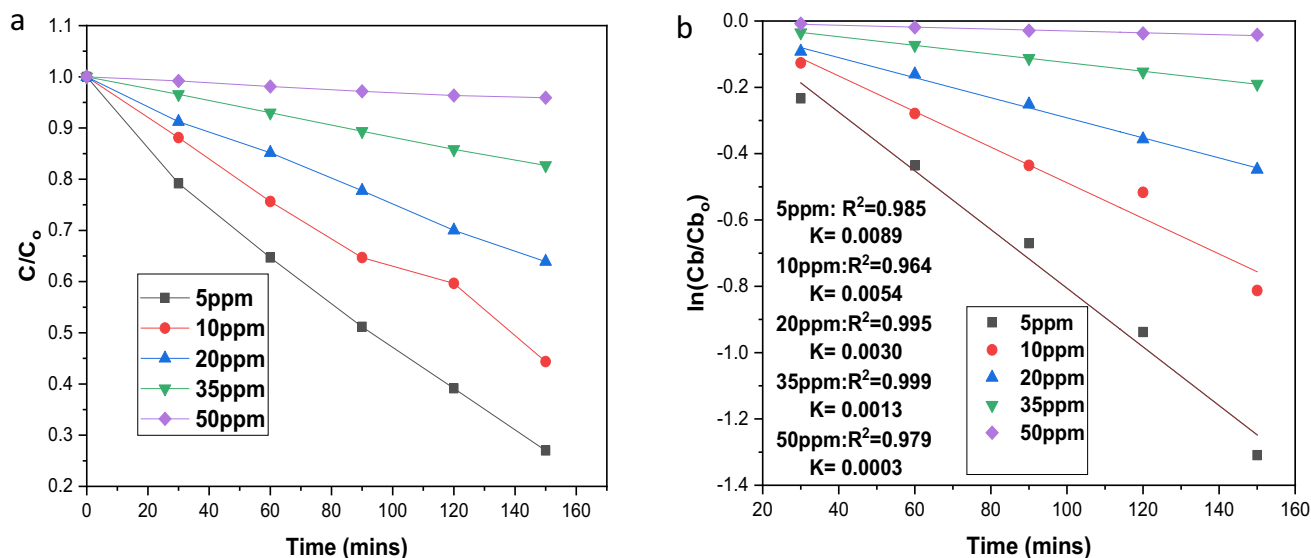


Fig. 7 **a** Influence of 2CBP concentration on the photodestruction; **b** Pseudo-first order plot for the photodestruction of the 2CBP at varying concentrations

Suggested photodestruction mechanism

The absorption of incident photons and effective charge migration at the interface can be improved by combining materials with diverse crystal lattices and energy band alignments. ZnO, an *n*-type semiconductor photocatalyst, has its Fermi level located near its conduction band, while BiOI, a *p*-type ternary metal oxide photocatalyst, has its Fermi level positioned close to its valence band (Zhang et al. 2020; Zhu et al. 2022). When BiOI is introduced into the ZnO crystal structure, a *p-n* heterojunction is formed, leading to an adjustment of the Fermi energy levels in both materials. This realignment leads to an inhibition in the resistance of surface carrier migration (Liu et al. 2021).

As presented in Fig. 6b, when BiOI with a low bandgap is exposed to visible light, its VB electrons are photoexcited to its CB. This excitation generates an internal electric field, which propels the photogenerated electrons on the *p*-BiOI's CB toward the *n*-ZnO. At the same time, the h^+ remains on the *p*-BiOI's VB. The effective migration of the photogenerated charge carriers and the consequent suppression of charge carrier recombination significantly boosts the performance of the ZnO-[10%]BiOI heterojunction (Tayyab et al. 2022; Yan et al. 2022). To achieve the optimum performance, controlling the concentration of dopant in the heterostructure is essential to align the thickness of the

charge layer and optical penetration depth. Additionally, the stoichiometry of the heterostructure and specific variation of dopants should be carefully controlled to ensure the effective separation of photoinduced charge carrier. Optimizing the doping concentration and controlling the stoichiometry and dopant variation is critical for achieving the best photocatalytic activity in heterostructures. This accounts for the reduction in the performance of the heterostructure beyond the optimum weight of 10% (Mohamed et al. 2023; Singh et al. 2021).

Influence of initial pollutant concentration

The impact of varying initial 2CBP concentrations (ranging from 5 to 50 ppm) on the photodegradation efficiency was examined by applying 35 mg of ZnO-[10%]BiOI composite. Results indicate that initial concentration has an influence in the photodestruction process, with photodegradation efficiency decreasing as initial 2CBP concentration increases (as shown in Fig. 7a). This is because, with increasing 2CBP concentration, more contaminant molecules will adhere to the surface of the photocatalyst, as exposure time to irradiation remains constant. Consequently, elevated initial contaminant levels can obstruct



the reaction sites of the heterojunction, which in turn inhibits the photon interaction with these sites. This finding provides evidence for the theory that a greater initial concentration of the pollutant may obstruct certain reaction sites on the photocatalyst, resulting in a decrease in photon interaction with those sites and a consequent deceleration in the destruction rate. Overall, the results suggest that controlling the initial concentration of 2CBP is crucial in optimizing the photocatalytic degradation process, as higher initial concentrations can lead to reduced photocatalytic activity.

Influence of catalyst dose

The catalyst weight (dose) applied in the photocatalytic process has a significant impact on pollutant degradation. To investigate this, the catalyst weight was varied (35, 70, 85, 100, and 150 mg) and evaluated for their effect on 2CBP degradation. Generally, raising catalyst concentration leads to a higher rate of organic pollutants' reduction due to increased hydroxyl radical generation from active sites. However, when the catalyst load is too high, particle–particle interaction can cause agglomeration and reduce the surface area available for light absorption, resulting in lower photocatalytic activity (Ahmed et al. 2011). While increasing the catalyst dose can create more active sites, excessive particle concentration reduces light penetration, causing an increase in turbidity and a reduction in photocatalytic activity (Malik et al. 2022). The formation of photogenerated electrons–holes and reactive oxygen species responsible for pollutant degradation benefits from a higher catalyst dose (Bahrami and Nezamzadeh-ejhieh 2015). However, an excessive amount of ZnO-[10%]BiOI can create opacity and a screening effect, which diminishes the surface area that is accessible for light harvesting and results in diminished photocatalytic performance.

Influence of pH

From the photodegradation plots, the heterojunction composite's poor performance in acidic conditions is due to the

agglomeration tendency of ZnO at low pH levels, leading to reduced pollutant adsorption and photon absorption. This can cause a lack of reaction sites on account of significant clustering of the anchored oxide, the data is presented in Table S3 (Bao et al. 2021). The degradation plots illustrated in Fig. S4a depict a decline in degradation efficiency in moderately acidic condition (pH 5; 34% destruction), a much more pronounced reduction in highly acidic condition (pH 2; 20%), and a considerably lower removal efficiency rate in alkaline condition (pH 9 = 10%; pH 11 = approximately 5%). The pH level of the solution has an impact on the adsorption of contaminant molecules on the surface of a photocatalyst (Li et al. 2010). This is because the solution's pH influences the photocatalyst's surface charge, the creation of hydroxyl radicals, and the deionization of contaminant molecules.

Kinetics study of the photodestruction process

The experimental results were analyzed using the apparent first-order reaction kinetics model (Fig. S5). The ZnO-[10%]BiOI, which exhibited the optimum performance in this investigation, displayed the best constant of 0.0054 min^{-1} . In comparison with the pure ZnO, the rate constant of the ZnO-[10%]BiOI material was almost five times greater, providing further evidence of the enhanced catalytic effectiveness of the ZnO-[10%]BiOI in this study. The kinetics data as presented in Table S1 indicate that it takes 128.4 min for the concentration of 2CBP to be reduced to half of the starting concentration when ZnO-[10%]BiOI is employed.

The analysis of the linear plots of the influence of pollutant concentration using the apparent-first-order kinetics confirms that the impact of the concentration of 2CBP on the removal process adheres to a pseudo-first-order kinetics (as illustrated in Fig. 7b). The rate constants and their corresponding R^2 values are presented in Table 2. The outcomes reveal that the degradation performance declines as the concentration of 2CBP rises. This can be accounted for by the fact that with increasing initial concentration of 2CBP, more of its molecules are adsorbed onto the surface of the ZnO-[10%]BiOI. Consequently, OH^\cdot radicals and O^{2-} anions generated on the surface of ZnO-[10%]BiOI at a constant irradiation get overloaded by the increasing number of 2CBP molecules, resulting in diminished removal efficiency. Furthermore, as the concentration of 2CBP increases, photons are obstructed before reaching the surface of ZnO-[10%]BiOI, which diminishes photon absorption and hence reduces photocatalytic efficiency.

Observations from the linear fits show that increasing the heterojunction photocatalyst weight from 35 to 70 mg resulted in an enhancement of the rate constant (0.0054 to 0.0089 min^{-1}) (Fig. S3b). However, when the catalyst weight was increased to 85 mg, a slight decrease was observed (from 0.0085 to 0.0077 min^{-1}). As displayed in Table S2,

Table 2 Influence of pollutant concentration

2CBP Concentration (ppm)	Performance (%)	K_{app} (min^{-1})	R^2
5	73	0.0089	0.985
10	57	0.0054	0.964
20	36	0.0030	0.995
35	17	0.0013	0.999
50	4	0.0003	0.979



a greater decline was observed when the loading exceeded 85 mg. This aligns with the photodestruction plot of 2CBP at different doses of the ZnO-[10%]BiOI heterostructure (Fig. S3a).

The influence of pH was fit into the pseudo-first order kinetic model. When the pH was increased to 9 and 11.3, the rate constant decreased significantly, by over sevenfold and 18-fold, respectively. When the pH was lowered to 5, the rate constant was halved, and it decreased even further when the pH was lowered to 2. These results suggest that the photocatalytic degradation of 2CBP is highly sensitive to changes in pH, with the reaction rate decreasing significantly as the pH deviates from the natural pH of 7.2. The best rate constant was obtained at pH of 7.2. The data is presented in Table S3.

Conclusion

This study reports the preparation of zinc oxide (ZnO), tungsten trioxide (WO₃), bismuth oxyiodide (BiOI) and the successful incorporation of varying loadings of WO₃ and BiOI into ZnO to form heterojunctions (ZnO-[X]BiOI and ZnO-[X]WO₃). The prepared photocatalysts and heterostructures were subsequently characterized and utilized for the photodegradation of 2CBP. The ZnO-[10%]BiOI heterojunction demonstrated the optimum photocatalytic performance in the destruction of 2CBP, with a rate constant nearly 5 times higher than undoped ZnO. The photodegradation reactions were modeled using pseudo-first-order kinetics to understand the photodegradation process better. The 2CBP concentration was found to impact the efficiency of the photodegradation, with higher initial concentrations resulting in lower degradation. Increasing the catalyst dose to 70 mg increased the rate constant (0.0054–0.0089 min⁻¹), while a decrease was observed at 85 mg (0.0085–0.0077 min⁻¹). The optimal pH for photodegradation was found to be 7.2, which is the natural pH of 2CBP for this study. The ZnO-[10%]BiOI heterojunction's improved photocatalytic performance was attributed to the effective migration of photoinduced charge carriers and inhibition of recombination. These findings suggest that ZnO-[10%]BiOI has the potential to serve as a potent and proficient catalyst to degrade obstinate and persistent organic contaminants in aqueous media.

Supplementary Information The online version contains supplementary material available at <https://doi.org/10.1007/s13762-023-05262-4>.

Funding Open access funding provided by University of the Witwatersrand.

Declarations

Conflict of interest The authors have no competing interests to declare relevant to this article's content.

Open Access This article is licensed under a Creative Commons Attribution 4.0 International License, which permits use, sharing, adaptation, distribution and reproduction in any medium or format, as long as you give appropriate credit to the original author(s) and the source, provide a link to the Creative Commons licence, and indicate if changes were made. The images or other third party material in this article are included in the article's Creative Commons licence, unless indicated otherwise in a credit line to the material. If material is not included in the article's Creative Commons licence and your intended use is not permitted by statutory regulation or exceeds the permitted use, you will need to obtain permission directly from the copyright holder. To view a copy of this licence, visit <http://creativecommons.org/licenses/by/4.0/>.

References

- Adhikari S, Sarkar D, Madras G (2015) Highly efficient WO₃-ZnO mixed oxides for photocatalysis. *RSC Adv* 5:11895–11904. <https://doi.org/10.1039/c4ra13210f>
- Ahmed S, Rasul MG, Brown R, Hashib MA (2011) Influence of parameters on the heterogeneous photocatalytic degradation of pesticides and phenolic contaminants in wastewater: a short review. *J Environ Manag* 92:311–330. <https://doi.org/10.1016/j.jenvman.2010.08.028>
- Ashiegbu DC, Moloto N, Potgieter J (2023) Improved photocatalytic activity of ZnO-[10%]BiOI and ZnO-[10%]WO₃ heterostructure in the destruction of 2-chlorobiphenyl. *Environ Sci: Adv*. <https://doi.org/10.1039/D2VA00222A>
- Ashiegbu DC, Potgieter JH, Kuvarega TA (2022) Synthesis of photocatalysts/heterojunctions for abatement of a specific pollutant in aqueous media. In: PhD Dissertation, University of the Witwatersrand
- Asilian H, Gholamnia R, Rezaee A, Jonidi A, Khavanin ALI (2010) Photochemical of polychlorinated biphenyl by the photolysis and solvent. *J Appl Sci Environ Manag* 14:107–112
- Bahrami M, Nezamzadeh-ejehieh A (2015) Effect of the supported ZnO on clinoptilolite nano-particles in the photodecolorization of semi-real sample bromothymol blue aqueous solution. *Mater Sci Semicond Process* 30:275–284. <https://doi.org/10.1016/j.mssp.2014.10.006>
- Bao HV, Dat NM, Giang NTH et al (2021) Behavior of ZnO-doped TiO₂/rGO nanocomposite for water treatment enhancement. *Surf Interfaces* 23:100950. <https://doi.org/10.1016/j.surf.2021.100950>
- Boruah PJ, Khanikar RR, Bailung H (2020) Synthesis and characterization of oxygen vacancy induced narrow bandgap tungsten Oxide (WO_{3-x}) nanoparticles by plasma discharge in liquid and its photocatalytic activity. *Plasma Chem Plasma Process* 40:1019–1036. <https://doi.org/10.1007/s11090-020-10073-3>
- Carey JH, Lawrence J, Tosine HM (1976) Photodechlorination of PCB's in the presence of titanium dioxide in aqueous suspensions.



- Bull Environ Contam Toxicol 16:697–701. <https://doi.org/10.1007/BF01685575>
- Dasary SSR, Saloni J, Fletcher A, Anjaneyulu Y, Yu H (2010) Photodegradation of selected PCBs in the presence of nano-TiO₂ as catalyst and H₂O₂ as an oxidant. *Int J Environ Res Public Health* 7:3987–4001. <https://doi.org/10.3390/ijerph7113987>
- Deng Y, Zhao R (2015) Advanced oxidation processes (AOPs) in wastewater treatment. *Curr Pollut Rep* 1:167–176. <https://doi.org/10.1007/s40726-015-0015-z>
- Gnanaprakasam A, Sivakumar VM, Thirumarimurugan M (2015) Influencing parameters in the photocatalytic degradation of organic effluent via nanometal oxide catalyst: a review. *Indian J Mater Sci* 2015:1–16. <https://doi.org/10.1155/2015/601827>
- Hong CS, Wang Y, Bush B (1998) Kinetics and products of the TiO₂ photocatalytic degradation of 2-chlorobiphenyl in water. *Chemosphere* 36:1653–1667. [https://doi.org/10.1016/S0045-6535\(97\)10040-6](https://doi.org/10.1016/S0045-6535(97)10040-6)
- Huang IW, Hong CS, Bush B (1996) Photocatalytic degradation of PCBs in TiO₂ aqueous suspensions. *Chemosphere* 32:1869–1881. [https://doi.org/10.1016/0045-6535\(96\)00080-X](https://doi.org/10.1016/0045-6535(96)00080-X)
- Ibhadon A, Fitzpatrick P (2013) Heterogeneous photocatalysis: recent advances and applications. *Catalysts* 3:189–218. <https://doi.org/10.3390/catal3010189>
- Jiang J, Wang H, Chen X et al (2017) Enhanced photocatalytic degradation of phenol and photogenerated charges transfer property over BiOI-loaded ZnO composites. *J Colloid Interface Sci* 494:130–138. <https://doi.org/10.1016/j.jcis.2017.01.064>
- Jing R, Fusi S, Kjellerup BV (2018) Remediation of polychlorinated biphenyls (PCBs) in contaminated soils and sediment: state of knowledge and perspectives. *Front Environ Sci* 6:1–17. <https://doi.org/10.3389/fenvs.2018.00079>
- Khatamian M, Khandar AA, Divband B et al (2012) Heterogeneous photocatalytic degradation of 4-nitrophenol in aqueous suspension by Ln (La³⁺, Nd³⁺ or Sm³⁺) doped ZnO nanoparticles. *J Mol Catal a: Chem* 365:120–127. <https://doi.org/10.1016/j.molcata.2012.08.018>
- Kumar SG, Rao KSRK (2015) Zinc oxide based photocatalysis: tailoring surface-bulk structure and related interfacial charge carrier dynamics for better environmental applications. *RSC Adv* 5:3306–3351. <https://doi.org/10.1039/c4ra13299h>
- Kumar SG, Rao KSRK (2017) Comparison of modification strategies towards enhanced charge carrier separation and photocatalytic degradation activity of metal oxide semiconductors (TiO₂, WO₃ and ZnO). *Appl Surf Sci* 391:124–148. <https://doi.org/10.1016/j.apsusc.2016.07.081>
- Lee KM, Lai CW, Ngai KS, Juan JC (2016) Recent developments of zinc oxide based photocatalyst in water treatment technology: a review. *Water Res* 88:428–448. <https://doi.org/10.1016/j.watres.2015.09.045>
- Li G, Li F, Zhang P et al (2010) Multiple effect of pH on photocatalytic degradation of orange II using TiO₂. *Adv Mater Res* 113–116:1878–1883. <https://doi.org/10.4028/www.scientific.net/AMR.113-116.1878>
- Liang Y, Martinez A, Hornbuckle KC, Mattes TE (2014) Potential for polychlorinated biphenyl biodegradation in sediments from Indiana Harbor and Ship Canal. *Int Biodeterior Biodegrad* 89:50–57. <https://doi.org/10.1016/j.ibiod.2014.01.005>
- Lin Y, Gupta G, Baker J (1995) Photodegradation of polychlorinated biphenyl congeners using simulated sunlight and diethylamine. *Chemosphere* 31:3323–3344. [https://doi.org/10.1016/0045-6535\(95\)00177-A](https://doi.org/10.1016/0045-6535(95)00177-A)
- Litter IM, Quici N (2011) Photochemical advanced oxidation processes for water and wastewater treatment. *Recent Pat Eng* 4:217–241. <https://doi.org/10.2174/187221210794578574>
- Liu Z, Hosseinzadeh S, Wardenier N et al (2019) Combining ozone with UV and H₂O₂ for the degradation of micropollutants from different origins: lab-scale analysis and optimization. *Environ Technol* 40:3773–3782. <https://doi.org/10.1080/09593330.2018.1491630>
- Liu Y, Zhu Q, Tayyab M et al (2021) Single-atom Pt loaded zinc vacancies ZnO–ZnS induced type-V electron transport for efficiency photocatalytic H₂ evolution. *Sol RRL* 5:1–10. <https://doi.org/10.1002/solr.202100536>
- Malik AQ, Mir TG, Amin O et al (2022) Synthesis, characterization, photocatalytic effect of CuS–ZnO nanocomposite on photodegradation of Congo red and phenol pollutant. *Inorg Chem Commun* 143:109797. <https://doi.org/10.1016/j.inoche.2022.109797>
- Mirzaeifard Z, Shariatnia Z, Jourshabani M, Rezaei Darvishi SM (2020) ZnO photocatalyst revisited: effective photocatalytic degradation of emerging contaminants using S-doped ZnO nanoparticles under visible light radiation. *Ind Eng Chem Res* 59:15894–15911. <https://doi.org/10.1021/acs.iecr.0c03192>
- Mohamed KM, Benitto JJ, Vijaya JJ, Bououdina M (2023) Recent advances in ZnO-based nanostructures for the photocatalytic degradation of hazardous. *Non-Biodegradable Medicines Crystals* 13:329. <https://doi.org/10.3390/cryst13020329>
- Osman AI, Elgarahy AM, Eltaweil AS et al (2023) Biofuel production, hydrogen production and water remediation by photocatalysis, biocatalysis and electrocatalysis. *Environ Chem Lett* 2023:1–65. <https://doi.org/10.1007/s10311-023-01581-7>
- Pirhashemi M, Habibi-Yangjeh A, Rahim Pouran S (2018) Review on the criteria anticipated for the fabrication of highly efficient ZnO-based visible-light-driven photocatalysts. *J Ind Eng Chem* 62:1–25. <https://doi.org/10.1016/j.jiec.2018.01.012>
- Qu Z, Su Y, Sun L et al (2020) Study of the structure, electronic and optical properties of BiOI/Rutile-TiO₂ heterojunction by the first-principle calculation. *Materials* 13:323. <https://doi.org/10.3390/ma13020323>
- Robertson LW, Weber R, Nakano T, Johansson N (2018) PCBs risk evaluation, environmental protection, and management: 50-year research and counting for elimination by 2028. *Environ Sci Pollut Res* 25:16269–16276. <https://doi.org/10.1007/s11356-018-2467-3>



- Singh J, Kumar D, Kumar PS et al (2021) Magnetically active Ag–Zn nanoferrites synthesized by solution combustion route: physical chemical studies and density functional theory analysis. *Mater Today Chem* 22:100588. <https://doi.org/10.1016/j.mtchem.2021.100588>
- Šrédlová K, Cajthaml T (2022) Recent advances in PCB removal from historically contaminated environmental matrices. *Chemosphere* 287:132096. <https://doi.org/10.1016/j.chemosphere.2021.132096>
- Tayyab M, Liu Y, Liu Z et al (2022) One-pot in-situ hydrothermal synthesis of ternary $\text{In}_2\text{S}_3/\text{Nb}_2\text{O}_5/\text{Nb}_2\text{C}$ Schottky/S-scheme integrated heterojunction for efficient photocatalytic hydrogen production. *J Colloid Interface Sci* 628:500–512. <https://doi.org/10.1016/j.jcis.2022.08.071>
- Wang Y, Hong CS, Fang F (1999) Effect of solution matrix on TiO_2 photocatalytic degradation of 2-chlorobiphenyl. *Environ Eng Sci* 16:433–440. <https://doi.org/10.1089/ees.1999.16.433>
- Wang J, Xia Y, Zhao H et al (2017) Oxygen defects-mediated Z-scheme charge separation in g- $\text{C}_3\text{N}_4/\text{ZnO}$ photocatalysts for enhanced visible-light degradation of 4-chlorophenol and hydrogen evolution. *Appl Catal B* 206:406–416. <https://doi.org/10.1016/j.apcatb.2017.01.067>
- Yan H, Wang X, Yao M, Yao X (2013) Band structure design of semiconductors for enhanced photocatalytic activity: the case of TiO_2 . *Prog Nat Sci: Mater Int* 23:402–407. <https://doi.org/10.1016/j.pnsc.2013.06.002>
- Yan G, Wang K, Jiang Z et al (2022) Flower-like ZnO/BiOI p–n heterojunction composites for enhanced photodegradation of formaldehyde and dyes. *J Mater Sci: Mater Electron* 33:23064–23074. <https://doi.org/10.1007/s10854-022-09073-0>
- Zhang P, Scudato RJ, Pagano JJ, Roberts RN (1993) Photodecomposition of PCBs in aqueous systems using TiO_2 as catalyst. *Chemosphere* 26:1213–1223. [https://doi.org/10.1016/0045-6535\(93\)90207-L](https://doi.org/10.1016/0045-6535(93)90207-L)
- Zhang C, Fei W, Wang H et al (2020) p–n Heterojunction of BiOI/ZnO nanorod arrays for piezo-photocatalytic degradation of bisphenol A in water. *J Hazard Mater* 399:123109. <https://doi.org/10.1016/j.jhazmat.2020.123109>
- Zhu Z, Guo F, Li A, Xu W, Zhang X (2022) Simple synthesis of BiOI/ZnO/rGO for efficient photocatalytic degradation of antibiotic chloramphenicol under visible light. *J Environ Sci* 2022:1–12. <https://doi.org/10.1016/j.jes.2022.05.045>

